Micron 202 (2026) 103981

Contents lists available at ScienceDirect

Micron

journal homepage: www.elsevier.com/locate/micron

# Morphometric analysis of axonal ultrastructure: Coordinated scaling of organelles and myelin

Vitalijs Borisovs [a,*], Mario Bossi [a], Guido Cavaletti [a,b]

[a] Experimental Neurology Unit, School of Medicine and Surgery, Università di Milano-Bicocca, Monza, Italy
[b] Fondazione IRCCS San Gerardo dei Tintori, Monza, Italy

ARTICLE INFO

*Keywords:*
Endoplasmic reticulum
Neuron
Electron microscopy
3D Reconstruction
Ultrastructure
Morphology

ABSTRACT

The endoplasmic reticulum (ER) is a crucial neuronal organelle involved in protein synthesis, calcium homeostasis, and metabolic support, essential for neuronal function and plasticity. Understanding its three-dimensional (3D) architecture is key to elucidating functional organization. Using SBF-SEM and AI-assisted segmentation, we established a quantitative framework to characterize ER and mitochondrial scaling within 35 peripheral nervous system (PNS) myelinated axons. Analysis of individual organelle morphometrics revealed a strong power-law relationship between surface area and volume for both mitochondria ($R^2 = 0.949$) and ER ($R^2 = 0.949$). The resulting exponents were super-isometric ($k_{Mito} = 0.85$, $k_{ER} = 0.73$), suggesting structural plasticity that prioritizes membrane surface expansion. A key finding was the distinction between size and number regulation: mitochondrial and ER volumes were negligibly correlated ($r \approx 0.03$), implying independent size regulation. However, organelle abundance (counts) showed a strong positive correlation ($r = 0.79$), maintaining an extremely low Bonferroni-adjusted Q value ($8.1 \times 10^{-9}$), suggesting coordinated control of organelle number in response to axonal size. Axonal populations were heterogeneous, with larger axons consistently containing more ER elements ($r = 0.59$) and mitochondria ($r = 0.69$). Furthermore, a low correlation of axon length with organelle content supports the idea that regulation is primarily a local phenomenon tied to cross-sectional size. These findings provide a quantitative basis for understanding how ER and mitochondria structurally adapt to axonal size, laying the groundwork for future research into how these scaling relationships influence neuronal metabolic health and contribute to neurological disease.

## 1. Introduction

The endoplasmic reticulum (ER) is an essential and highly compartmentalized organelle in neurons, coordinating crucial functions including protein synthesis and folding (Hetz, 2012), lipid metabolism (Vance, 2014), and the regulation of intracellular calcium (Ca2 +) signalling (Clapham, 2007). The ER's structure is specialized across neuronal domains: the dendritic spine apparatus supports local Ca2 + dynamics (Dittmer and Dell'Acqua, 2024; Maiellano et al., 2023a), while the RER in the soma supports high protein synthesis (Verkhratsky, 2004). The axonal ER, characterized by a tubular network, is increasingly recognized for its role in transport and maintenance (Kuijpers et al., 2024).

Traditional 2D TEM provided fundamental ultrastructure knowledge (Sree et al., 2021), but it limits understanding of the complex three-dimensional (3D) architecture necessary for ER function. Resolving this requires advanced volumetric imaging techniques like Serial Block Face – Scanning Electron Microscopy (SBF-SEM) (Denk and Horstmann, 2004) and Focused Ion Beam Scanning Electron Microscopy (FIB-SEM) (Kasthuri et al., 2015). These methods are crucial for resolving true organelle morphology and contacts, often obscured in 2D views. Ongoing advancements, including improved reconstruction algorithms and AI-assisted segmentation, are further enhancing the ability to analyse large-scale datasets with greater precision and efficiency (Tafti et al., 2015; Jiang et al., 2025).

A critical aspect of ER function is its close apposition to mitochondria at Mitochondria-Associated Membranes (MAMs), vital sites for Ca2 + signalling and lipid transfer (Rowland and Voeltz, 2012). 3D EM is a powerful tool to investigate the structural basis of MAMs in axons, especially given their potential dysregulation in neurodegenerative conditions (Wu et al., 2018).

This study utilizes 3D SBF-SEM and AI-assisted segmentation to

* Corresponding author.
*E-mail address:* vitalijs.borisovs1@unimib.it (V. Borisovs).

https://doi.org/10.1016/j.micron.2025.103981
Received 9 September 2025; Received in revised form 16 November 2025; Accepted 8 December 2025
Available online 8 December 2025

establish a quantitative framework for analyzing axonal organelle organization in the peripheral nervous system (PNS). We aim to quantify the ER's 3D architecture, characterize its interaction sites with mitochondria (MAMs), and statistically analyze the relationships between ER/MAM morphology and the geometric parameters of axons. By providing these detailed 3D insights and quantitative correlations, this work seeks to deepen our knowledge of neuronal structure and the implications of ER alterations in neurological disorders.

## 2. Materials and methods

### 2.1. Tissues processing

In compliance with the 3 R's principles aimed at the reduction of animal use for experimental studies (Lauwereyns et al., 2024), healthy Balb/c mice (Envigo, San Pietro al Natisone, Italy) belonging as controls to a study conducted in conformity with the institutional guidelines in compliance with national (D. L.vo 26/2014, Gazzetta Ufficiale della Repubblica Italiana, n.61, 14 March 2014) and international laws and policies (European Union directive 2010/63/UE; Guide for the Care and Use of Laboratory Animals, U.S. National Research Council, 1996), and approved by the Italian Ministry of Health (approval n. 777/2022-PR) were used. Intracardiac perfusion was performed in animals under deep anesthesia with Ketamine/Xylazine using a peristaltic pump (Heidolph Pumpdrive 5101, Biosigma, Cona, Venice, Italy). An 18-gauge needle was inserted into the left ventricle at an angle approximately parallel to the midline of the heart, then a small incision was made in the right atrium. Immediately after the venous blood (7 mL) escaped from the right atrium, perfusion with sterile saline solution was started at a constant speed of approximately 1 mL/5 s, to clean the vascular tree. The animals were then perfused with 150 mL of 4 % paraformaldehyde, at the same constant rate. Subsequently, nerves were dissected out and immediately immersed in 3 % glutaraldehyde diluted in 0.15 M sodium cacodylate buffer for 3 h for a further fixation. Nerves were cut into small pieces (approx. 5 mm) with a razor blade to help the samples to fit inside the baskets of the automatic staining instrument and the staining solutions to penetrate homogeneously within tissue volume.

### 2.2. Uranyl acetate-free en bloc staining with automated processor

The samples were processed with the Leica EM TP 1020 Automated Tissue Processor (Leica Biosystems, Buccinasco, Italy). Processing schedule was inspired by Moscardini et al. published protocol (Moscardini et al., 2020) with modifications. The so-called X-solution required by the method was produced in our laboratory following the description from the article. After specimen fixation was performed, samples were separately inserted into porous baskets with phosphate buffer and incubated for two times 10 min each. Successively, 0.12 M sodium cacodylate buffer (pH 7.4) was used to wash the samples for two times (10 min each) prior to the post-fixation in 1 % potassium ferricyanide $K_3[Fe(Cn)_6]$-reduced 1 % osmium tetroxide for 1 h and 45 min at room temperature. The specimens were then washed twice in 0.12 M sodium cacodylate buffer and again in bidistilled water (each step for 10 min). Samples were then conditioned in 20 % ethanol for 10 min before being impregnated with X-solution for 1 h at room temperature. Gradual ethanol dehydration (20 %, 50 %, 70 %, 96 %, two steps in 100 %, 10 min each step) was then performed at room temperature. Samples were subsequently impregnated in 100 % propylene oxide for 10 min and gradually embedded in epoxy resin Embed 812 (Electron Microscopy Sciences, USA) with propylene oxide and resin balanced mixture (75 %, 50 %, 25 % and 0 %, respectively) for 30 min each step, at room temperature. The hard resin formulation was used. Resin-embedded specimens were finally transferred into molds, and the resin polymerized at 60° C for 48 h.

### 2.3. From block to sample mounting

Semi-thin (1–1.5 μm) sections from the block face were collected, stained with toluidine blue, and examined under a conventional bright field optical microscope for structural integrity check and selection of the region of interest (ROI); ultrathin (approx. 70 nm) sections were checked using a Hitachi TEM HT7800 (Hitachi High-Tech Europe GmbH, Krefeld, Germany) before proceeding to sample mounting and SBF-SEM imaging, to ensure the quality of the staining. The block face was, hereafter, trimmed with a razor blade to create a truncated square pyramid (approx. 500 μm x 500 μm x 2 mm) with the ROI near its center and to remove the empty resin which increases the build-up of negative charges on the surface during the imaging. Pyramid was then dislodged and mounted onto an aluminum pin using a drop of pre-cured embedding resin as glue. Resin drop was left polymerizing overnight in the oven at 60°C to ensure sample-pin anchoring. Specimen surface was again smoothed with the diamond knife, to produce a flat block face and reduce any possible small tilts with the diamond knife of the in-chamber ultramicrotome. Finally, mounted samples were sputter-coated with a fine nm-layer of gold palladium using a Vac Coat DSCT sputter coater device (Vac Coat Ltd., London, UK) and the aluminum pin base and block edges were covered with a small amount of silver paste before the insertion into the SBF-chamber.

### 2.4. High resolution 3D imaging via SBF-SEM

Cubic microns of imaging data were achieved using a Zeiss Gemini SBF-SEM 360 (Carl Zeiss S.p.A., Milan, Italy) equipped with the in-chamber ultramicrotome Volutome, and piloted by the Volutome software package, which fully assists the slicing and imaging cycle with minimal user involvement. The sample used was a single segment of Balb/c mouse sciatic nerve.

The cutting cycle was fixed to a nominal speed of 0.1 mm/s and a thickness of 50 nm for every cycle, thus determining the axial resolution as well as the voxel size. High-resolution acquisitions of the resin block faces were performed using a 30 μm beam aperture and the Volutome backscattered electron (BSD) detector.

Imaging was performed in BSD mode with the following parameters: 1.75 kV (accelerating voltage), 6 nm/pixel (in-plane resolution), 1 μs (dwell time), and 65 % FCC (Focal Charge Compensation), resulting in an approximate electron dose of 40 e/nm$^2$.

The resulting dataset comprised 353 sections, yielding a total axial thickness of 17.65 μm (353 sections×50 nm). The Field of View (FOV) was approximately 22 μm× 22 μm (~500 μm$^2$).

Within this volume, only 35 myelinated axons were selected and reconstructed for analysis. Schwann cells and their associated cytoplasm were excluded from segmentation as they were not relevant to the study goals.

Optimum imaging conditions were adjusted depending on sample contrast and conductivity. Nitrogen gas injection through the focal charge compensation system (FCC) was systematically used to mitigate negative charging and improve cutting performance.

### 2.5. Image analysis and 3D rendering

Segmentation, deep learning models, final 3D rendering and downstream analysis of tissue ultrastructures were accomplished via Zen Arivis Vision4D (Carl Zeiss S.p.A., Milan, Italy). The fully automated approach was chosen to post-process different sample acquisitions. Therefore, for each tissue compartments (i.e., myelin sheaths, endoplasmic reticulum mitochondria), deep learning (DL) models were devised by manually tracing the structures of interest with the brush tool; generally, up to 100 annotations were needed for data segmentation. DL segmenters were then combined into an additional feature filter to remove incorrectly labeled objects prior to the 3D reconstruction.

### 2.6. Statistical analysis

All quantitative analyses were performed using Python 3 and its associated libraries: matplotlib, numpy, seaborn, scipy, and pandas.

### 2.7. Geometric and morphological calculations

Axon geometry parameters, including length, cross-sectional area, inner axon diameter (r), fiber diameter (R), and myelin thickness, were calculated directly from the 3D reconstructed segmentations of the myelin and axon. The g-ratio for each axon was calculated using the conventional formula: g-ratio = r/R.

### 2.8. Data characteristics and distribution

Prior to parametric testing, data normality was assessed using the Shapiro-Wilk test, and homogeneity of variances was assessed using the Levene test. Depending on the results of these tests and the nature of the data, the appropriate statistical comparison was chosen between the Mann-Whitney *U* test (for non-parametric data) and the Student's *t*-test (for parametric data).

### 2.9. Correlation and robustness analysis

Correlations between continuous variables (axonal, mitochondrial, and ER morphometrics) were identified using both Pearson and Spearman correlation coefficients. The complete correlation matrix (see Supporting Information) involved a large number of comparisons; therefore, the resulting p-values were corrected for multiple comparisons using a Bonferroni procedure to maintain statistical rigor and report the Bonferroni-adjusted Q values.

To confirm the stability and reliability of the key correlation coefficients (e.g., between organelle counts), a bootstrap resampling analysis was performed. This involved repeatedly resampling the dataset with replacement (10 000 iterations) to generate empirical 95 % confidence intervals.

### 2.10. Scaling analysis

The intrinsic relationship between organelle volume and surface area, as well as the relationship between organelle density and axon size, was characterized using power-law regression. This involved transforming the data to a log-log scale and applying a linear fit, where the slope of the fit was interpreted as the power-law exponent (k). The statistical significance of these exponents was tested against the null hypothesis (e.g., isometric scaling) and validated using the Bonferroni-adjusted Q values.

## 3. Results

A randomly selected sample of sciatic nerve was imaged (Fig. 1A) with a z-stack consisting of 353 images (Fig. 1B). For the given purpose of studying the interaction between axonal ER and mitochondria, Schwann's cell reconstruction was not relevant, so only myelin, axonal ER and mitochondria were reconstructed for 35 myelinated fibres axons (Fig. 1C).

A Deep Learning model with 3 annotated classes and Intersection over Unit (IoU) score of 89.19 % was able to fully reconstruct each individual axon (Fig. 2A). Movies 1 and 2 in supplementary materials provide a more detailed 3D view of the reconstructed axon. Myelin was usually the most well-defined structure of the axon. The segmentation and reconstruction of myelin (Fig. 2B) did not pose a challenge both for Machine and Deep learning algorithms. 3D reconstruction of intra axonal mitochondria (Fig. 2C) was similarly feasible but requiring significantly more annotations during the model preparation step. Reconstructed 3D structures of intra axonal mitochondria tended to lack structural integrity and uniformity due to their interaction with ER. By contrast, axonal ER was extremely difficult to segment. With the varying size and morphology of each segment, the axonal ER reconstruction required a pixel-size precision. Despite this difficulty, it was possible to obtain a near perfect 3D reconstruction of the axonal ER (Fig. 2D) showing that it has a structure that resembles a network of tubular segments with varying size.

The main observation here is that the interaction points between axonal ER and mitochondrion gave rise to large 'bubble-like' formations (Fig. 3A). When reconstructed, there was a noticeable change in shape of mitochondria and the abnormally large segments of ER (Fig. 3B).

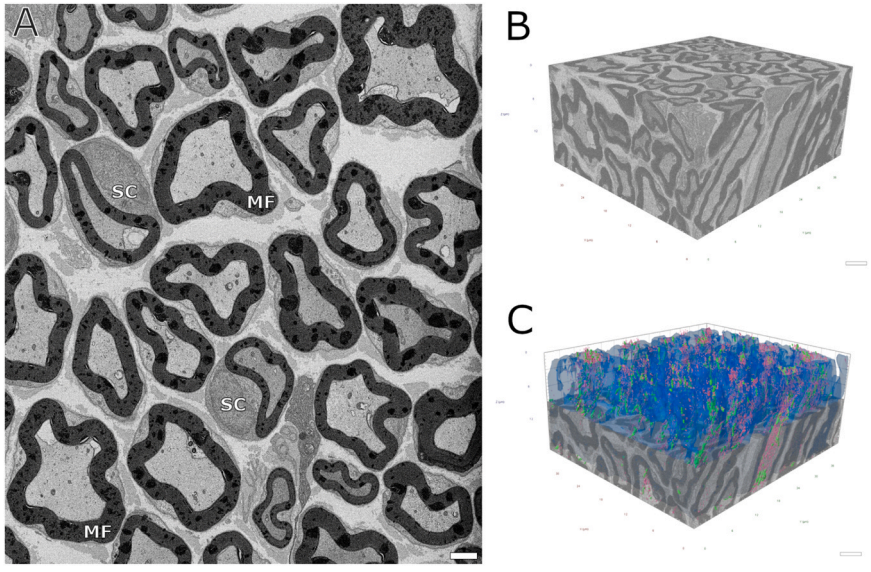


**Fig. 1.** A: Sciatic nerve micrograph (obtained in BSD mode, 1.75 kV, 6 nm pixel size, 1 µs as dwell time, 65 % FCC, approx. 40 e/nm$^2$). MF - myelinated fibres, SC - Schwann's cells. Scale bar: 2 µm; B: Sciatic nerve sample 3D block with 353 stacks 50 nm each (17.65 µm total thickness). Scale bar: 500 µm; C: Reconstructed sciatic nerve sample 3D block with myelin in blue, mitochondria in green, endoplasmic reticulum in magenta (colour coding remains the same throughout the whole manuscript). Scale bar: 500 µm.

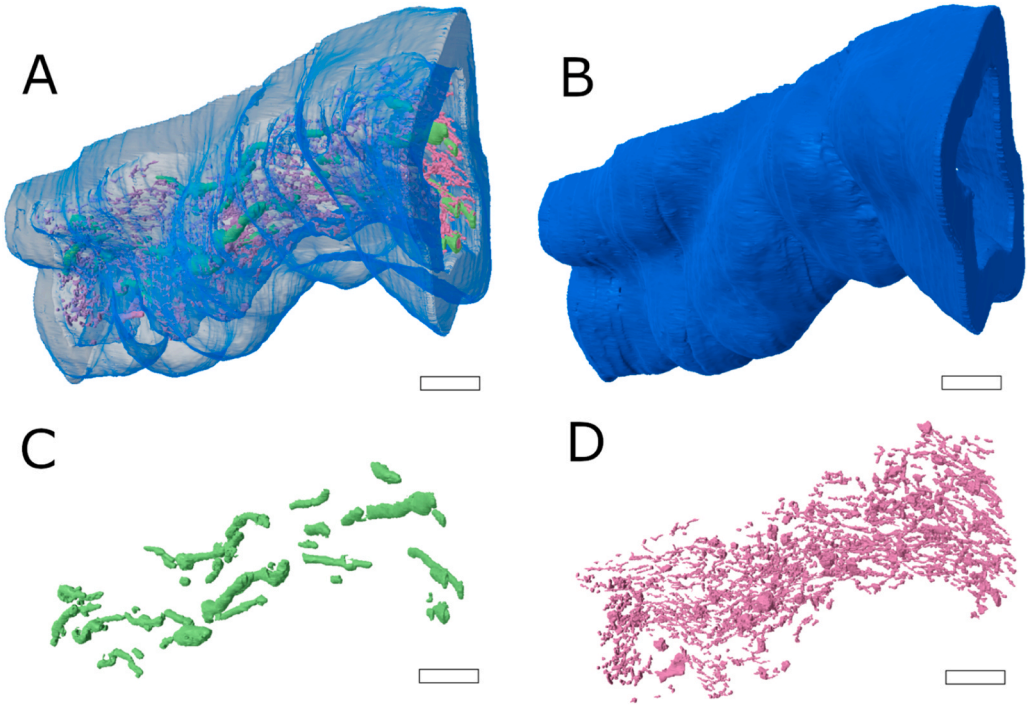


**Fig. 2.** 3D reconstructed single axon of the sciatic nerve. A – full reconstruction of a single axon of the sciatic nerve. Myelin with transparency mode on for better visualisation, B – reconstructed myelin, C – reconstructed mitochondria, D – reconstructed endoplasmic reticulum. Scale bar: 1 μm.

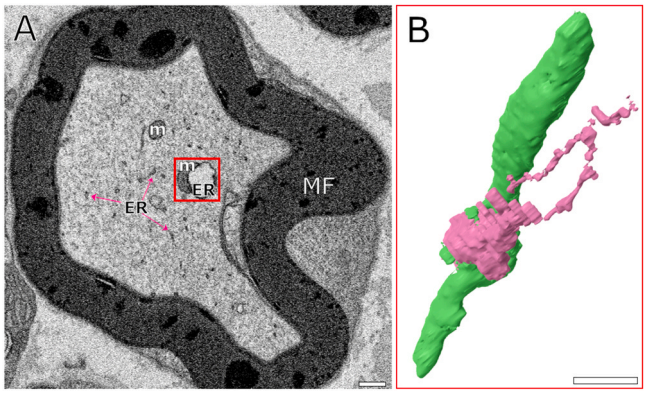


**Fig. 3.** A: A single axon of the sciatic nerve with MF – myelinated fibre, m – intra axonal mitochondria, ER – endoplasmic reticulum. Scale bar: 500 nm. Red box indicates an area of interest for the 3D reconstruction. B – a 3D reconstruction of the interaction between a single intra axonal mitochondrion (green) and endoplasmic reticulum (magenta). Scale bar: 500 nm.

### 3.1. Axon geometry and morphology evaluation

To move beyond the raw values and understand the underlying characteristics of the population, violin plots (Fig. 5) were generated to visualize the probability density of the four key morphometric parameters. The g-ratio has a certain degree of variability as it was seen from the bar plot (Fig. 4A), yet the violin plot (Fig. 5A) indicate peaked distribution, with a high concentration of axons falling near the theoretical optimal range of 0.5 – 0.6 (nearly identical mean and median values – 0.548 and 0.546 in Table 1). This suggests that a majority of the myelinated fibres in the sample are structurally optimized for efficient nerve conduction. However, the distributions for axon radius (Fig. 5B), exhibit a distinctive right-skew with mean value (1.572 μm) being slightly greater than median value (1.536 μm). This observation indicates that the sample population is dominated by a high density of smaller axons, with a long, sparse tail extending to include a small number of axons with significantly larger radii and thicker myelin sheaths.

In contrast median values (Table 1) of fiber radius and myelin thickness (2.973 μm and 1.290 μm) are slightly higher than mean values (2.842 μm and 1.269 μm) which results a slightly left-skewed distribution (Fig. 5C and D). This suggests a dynamic and complex scaling relationship, where the growth of the insulating myelin sheath and the resulting total fiber diameter do not scale in a simple, linear fashion with the underlying axon diameter.

### 3.2. Correlation analysis of axonal and organellar morphometrics

The full matrix of Pearson correlation coefficients among all structural and morphological variables related to mitochondria (Mito), ER, and axons is presented in the Supporting Information (Figure S1), with key axon-wise findings illustrated in Fig. 6A.

### 3.3. Organelle morphometrics

A strong positive correlation was observed between mitochondrial surface area and mitochondrial volume ($r = 0.97$), as well as between ER surface area and ER volume ($r = 0.96$). However, parameters related to organelle size showed negligible correlation between the two organelles, with coefficients near zero between mitochondrial volume or surface area and their ER counterparts (r ranging from 0.03 to 0.04).

In contrast, mitochondrial and ER counts showed a strong positive correlation ($r = 0.79$). Mitochondria count showed a strong correlation with axon inner volume ($r = 0.69$) and axon total volume ($r = 0.73$). ER count showed a significant correlation with axon inner volume ($r = 0.59$) and axon total volume ($r = 0.64$).

### 3.4. Geometric and length correlations

The correlation between myelin thickness and g-ratio was negative ($r = -0.32$). The correlation between axon radius and myelin thickness

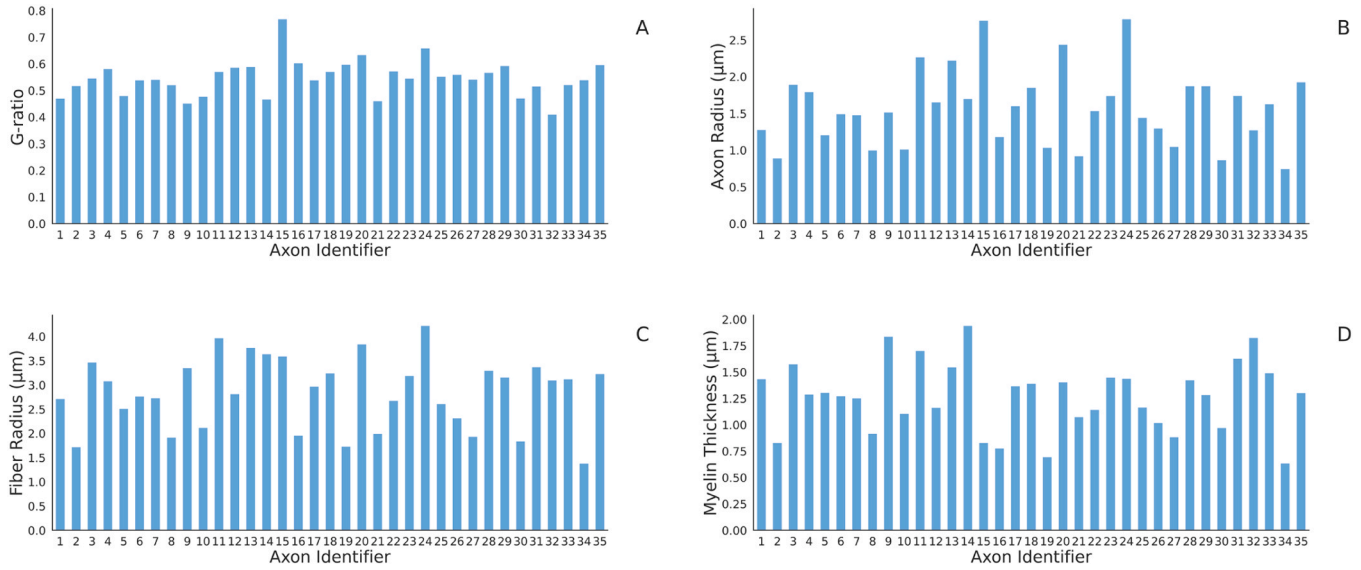


**Fig. 4.** Bar plots illustrate axon-by-axon view of key morphological parameters, including g-ratio (A), axon radius (B), fibre radius (C), and myelin thickness (D), for the 35 myelinated fibres in the sample. This reveals a high degree of morphological heterogeneity across the nerve sample, a finding that is consistent with the known composition of peripheral nerves, which contain a mix of different fibre variations to support a range of signal conduction velocities. The axon radius is shown to vary significantly, with some axons measuring less than 1.0 µm in radius while others approach 3.0 µm. Similarly, myelin thickness exhibits considerable variation, ranging from ~ 0.7 µm to almost 2.0 µm.

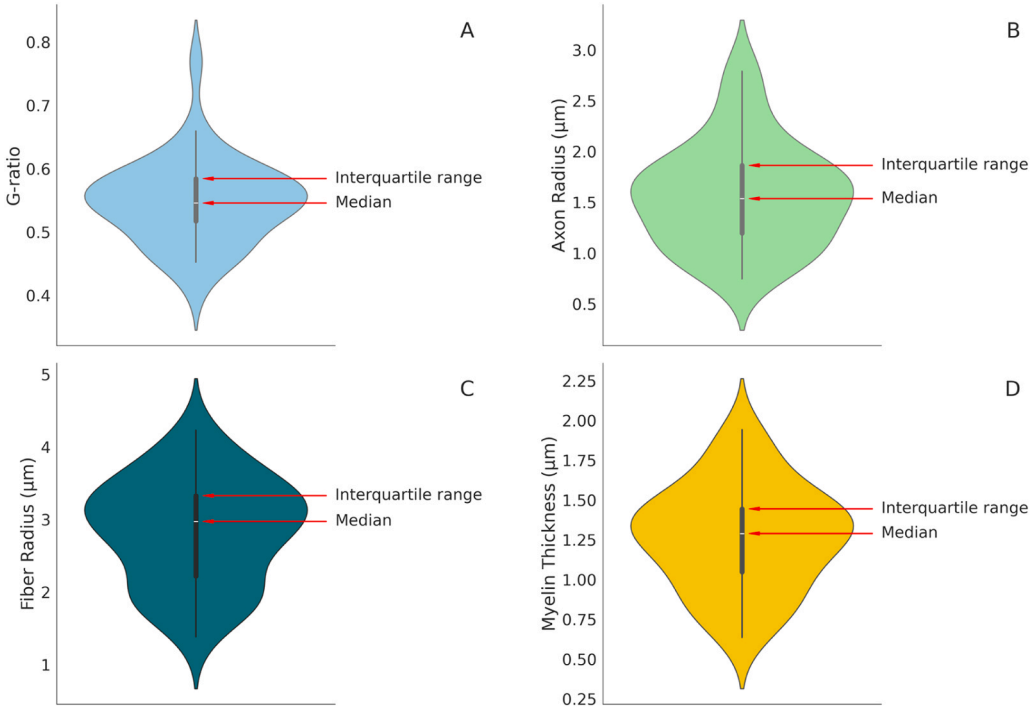


**Fig. 5.** Violin plots of key axonal parameter statistical distribution. A – g-ratio distribution; B – axon radius (inner radius) distribution; C – fiber radius distribution; D – myelin thickness distribution.

**Table 1**
Descriptive statistics of key axonal morphometric features.

| Parameter | Mean | Median | SD | IQR |
|---|---|---|---|---|
| g-ratio | 0.548 | 0.546 | 0.067 | 0.067 |
| Axon Radius (µm) | 1.572 | 1.536 | 0.515 | 0.667 |
| Fiber Radius (µm) | 2.842 | 2.973 | 0.727 | 1.108 |
| Myelin Thickness (µm) | 1.269 | 1.290 | 0.328 | 0.397 |

was strong and positive ($r = 0.78$), whereas the correlation between axon radius and fiber radius was higher ($r = 0.92$).

A key finding was the low correlation of axon length with nearly all other parameters. For instance, the correlation between axon length and myelin volume was $r = 0.46$, and between length and ER volume was $r = 0.07$.

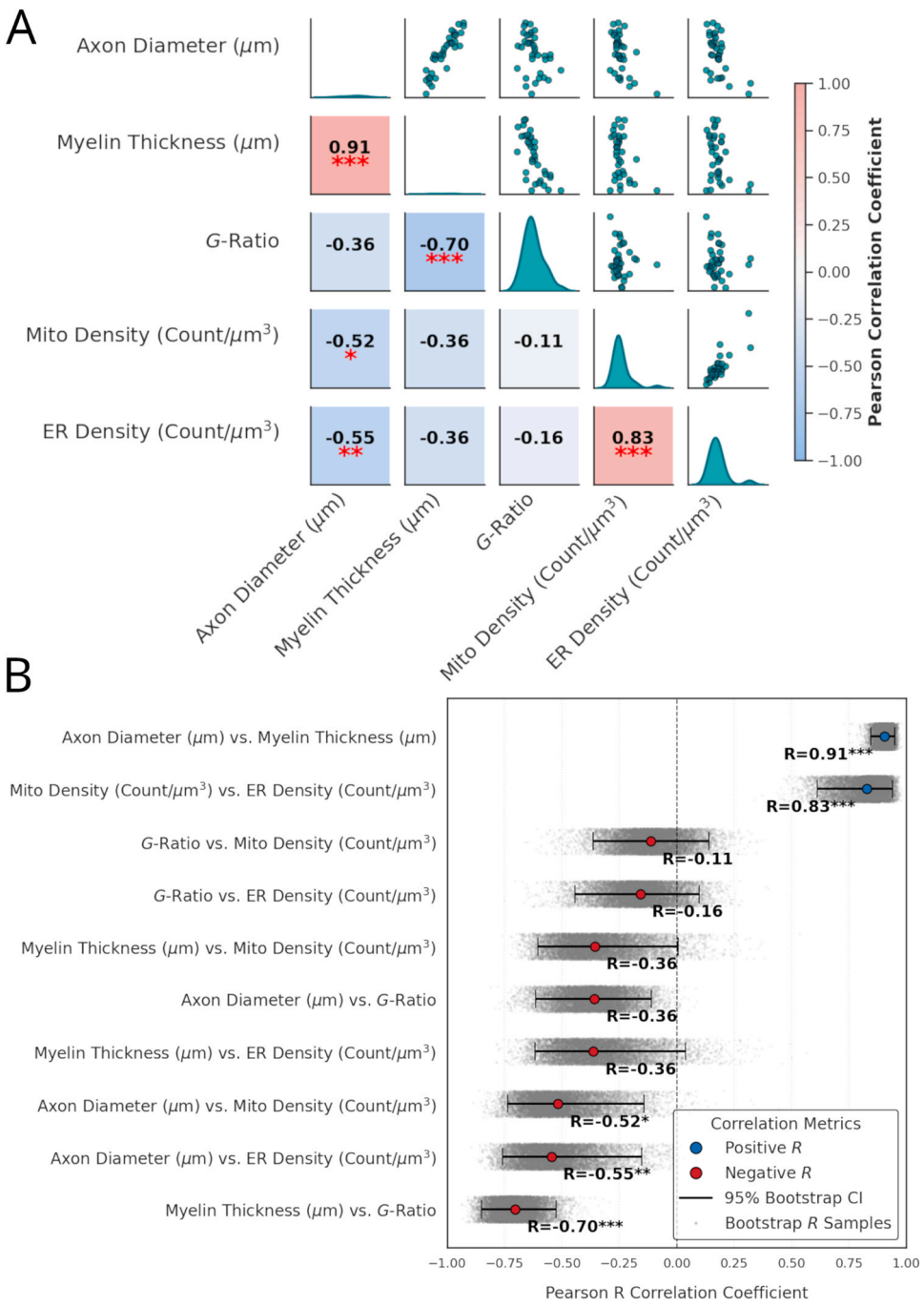


**Fig. 6.** A: Pearson Correlation Matrix and Pair-Dot Plots. Correlation heatmap (bottom half) and pair-dot plots (top half) illustrating the relationships among key geometric parameters of the axons (radius, thickness, volume, length) and the structural metrics of mitochondria (Mito) and Endoplasmic Reticulum (ER).

### 3.5. Robustness check

The bootstrap analysis shown in Fig. 6B was performed to confirm the statistical reliability of the calculated Pearson correlation coefficients, given the limited sample size of 35 axons. This method involved repeatedly resampling the data with replacement and recalculating the correlation coefficients (10000 times). The narrow distribution of the resulting bootstrap estimates (the 95 % confidence intervals shown in Fig. 6B) demonstrates the stability and consistency of the key relationships observed in the full dataset. Specifically, the clear separation of the confidence intervals for the organelle count correlation ($r = 0.79$) from zero confirms the statistical robustness of the co-scaling relationship between mitochondrial and ER abundance across the axon population.

B: Bootstrap Analysis of Key Correlation Coefficients. Distribution and 95 % confidence intervals (CI) of Pearson coefficients calculated via bootstrapping (resampling the dataset 1000 times). This analysis confirms the statistical robustness and reliability of the primary correlations, particularly the co-scaling observed between mitochondrial and ER counts, which is demonstrated by the CI being clearly separated from zero.

Fig. 7A illustrates the intrinsic scaling relationship between surface area and volume for individual mitochondria and ER elements within the analyzed axons. To capture this relationship rigorously, the data were plotted on a log-log scale, where a linear fit corresponds to a power-law model ($Y \sim X^k$).

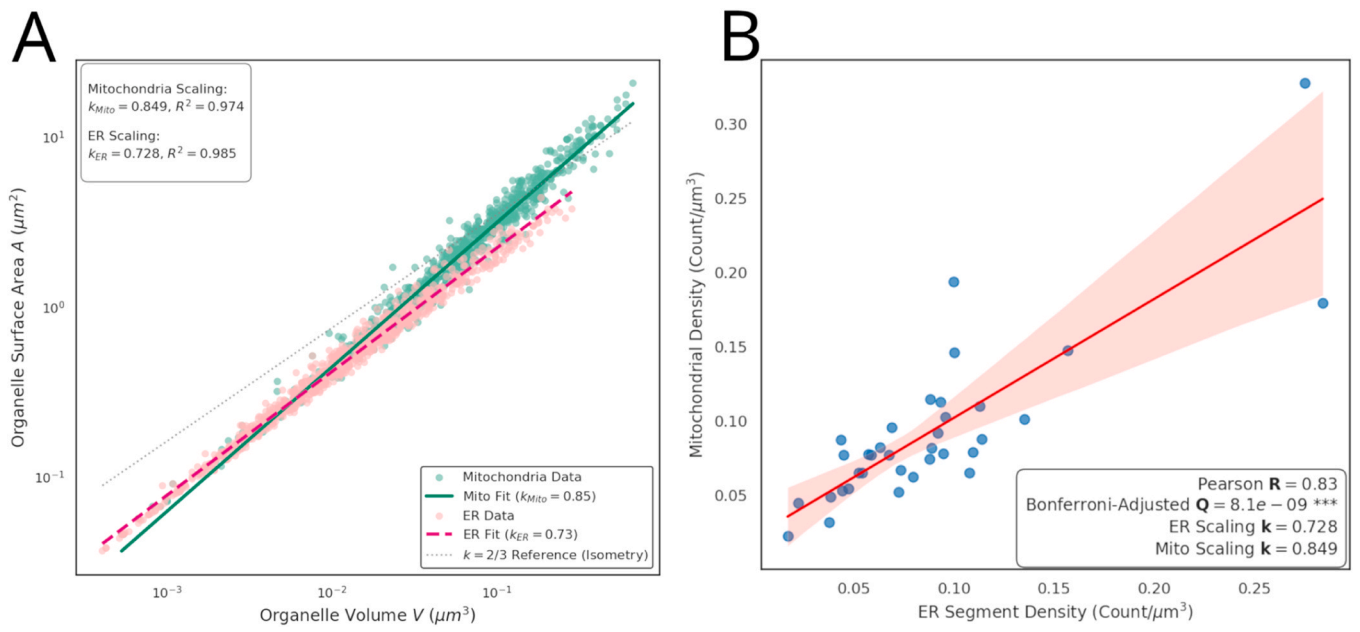


**Fig. 7.** A: Scatter plots illustrating the intrinsic power-law scaling between the measured volume (μm$^3$) and total surface area (μm$^2$) for individual mitochondria (green) and Endoplasmic Reticulum (ER) elements (pink) across all 35 analyzed axons. The data is plotted on a log-log scale, where the linear fit represents the power-law relationship ($Y \sim X^k$).

For both organelles, a clear, strong power-law relationship was observed, confirming that as the volume of an organelle increases, there is a predictable corresponding increase in its surface area. The high coefficient of determination ($R^2$) observed for both mitochondria ($R^2$=0.949) and ER ($R^2$ = 0.949) indicates that the power-law model accounts for approximately 95 % of the variability in the surface area measurements, establishing the fit as highly representative of the observed structural scaling.

The power-law exponents (the slope, k) derived from these fits were found to be $k_{Mito} = 0.85$ for mitochondria and $k_{ER} = 0.73$ for the ER. An exponent greater than the isometric value ($k \approx 0.67$ for surface area *vs.* volume) suggests a tendency toward super-isometric expansion of membrane surface relative to volume as the organelle size increases. This structural trend may indicate a tendency toward a more elongated, branched, or complex morphology, optimizing the membrane surface area critical for function.

The statistical significance of these (Fig. 7B) exponents was tested using methods that account for multiple comparisons (Bonferroni correction). Although the specific Bonferroni value (or threshold) is not listed here, applying such a correction is necessary to maintain the false discovery rate when fitting multiple models simultaneously. This procedural rigor ensures that the reported exponents for $k_{Mito}$ and $k_{ER}$ represent statistically valid deviations from isometric scaling, rather than being artifacts of random chance.

The scatter of individual data points around the fitted power-law line, particularly at higher volumes, indicates inherent variability in organelle shape. The higher density of data points at smaller volumes suggests that smaller mitochondria and ER elements are more prevalent in the sample.

B: Scatter plot illustrating the relationship between Mitochondrial Density (Count per μm$^3$) and ER Segment Density (Count per μm$^3$) across all individual myelinated axons analyzed. The red line represents the linear regression fit, with the shaded area showing the 95 % confidence interval. The strength of the linear relationship is indicated by the Pearson R value of 0.83. The statistical significance of this correlation is confirmed by the Bonferroni-adjusted Q value of $8.1 \times 10^{-9}$.

### 3.6. Mitochondria and ER mean surface area and volume comparison

The bar graphs presented in Fig. 8 and Fig. 9 provide a direct comparison of the mean surface area and mean volume, respectively, of mitochondria and ER segments within the analysed axons.

Fig. 8 illustrates that the mean mitochondrial surface area was approximately 2.75 μm$^2$, which is significantly larger than the mean ER surface area, recorded at approximately 0.75 μm$^2$. Similarly, as shown in Fig. 9, the mean mitochondrial volume was substantially greater, around 0.085 μm$^3$, compared to the mean axonal ER volume of about 0.025 μm$^3$. These findings collectively demonstrate that, on average individual mitochondria occupy a considerably larger physical space and present a greater surface area within the axon compared to individual ER elements. This observation is consistent with the high energy

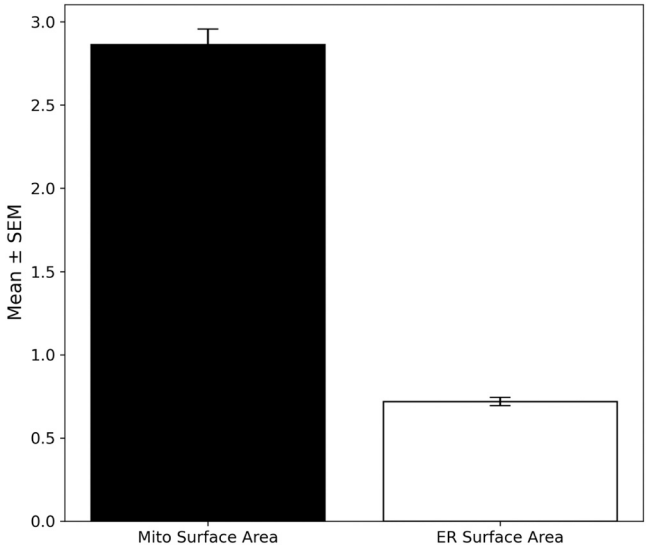


**Fig. 8.** The comparison of mitochondrial and ER segments surface areas. The error bars on both graphs, representing the standard error of the mean (SEM), indicate the variability within each group.

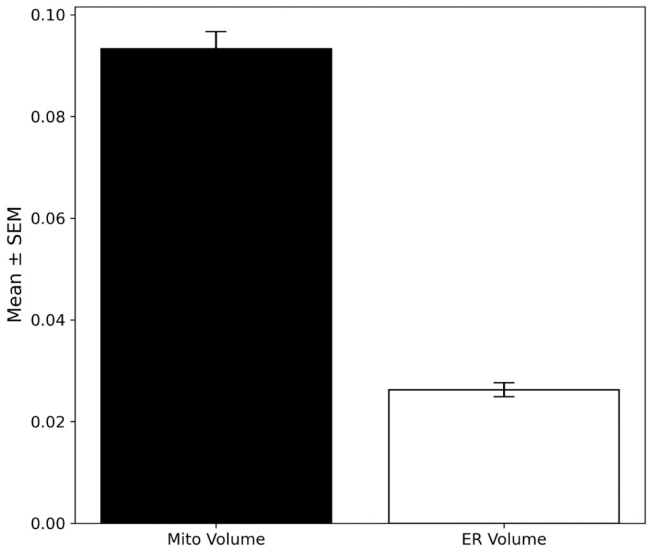


**Fig. 9.** The comparison of mitochondrial and ER segments volumes. The error bars on both graphs, representing the standard error of the mean (SEM), indicate the variability within each group.

of the axon, where mitochondria serve as the primary powerhouses, necessitating a larger volume and extensive internal surface area for efficient ATP production. In contrast, the smaller average size of ER elements, despite potentially higher counts in larger axons as suggested by previous correlations, aligns with its more distributed role in localized calcium buffering, lipid synthesis, and other signalling events along the axonal length, which do not require the same volumetric or surface area capacity as energy generation. The distinct differences in mean size and surface area between these two organelles underscore their specialized and complementary role in maintaining neuronal physiology.

## 4. Discussion

Volumetric EM has previously offered insights into ER architecture and its relationships with other organelles in various neuronal compartments, such as dendritic spines (Maiellano et al., 2023b). Prior work using 3D reconstructions has systematically examined membrane apposition involving the ER (at distances $\leq$30 nm) across dendrites, axons, and terminals, suggesting ER contacts with mitochondria, where the axonal ER sometimes appears to form embracing networks (Wu et al., 2017). Structural details concerning ER components, like membrane-associated ribosomes, have also been revealed using advanced techniques like cryoelectron tomography (Pfeffer et al., 2012). Recent methodological advances, including automated 3D reconstruction using deep learning (Liu et al., 2020) and Automatic Tape-collecting Ultra-Microtome Scanning Electron Microscopy (ATUM-SEM) studies, have further highlighted the ER's substantial surface area and its contacts with mitochondria (Jiang et al., 2021). While previous studies successfully visualized ER-mitochondria apposition and axonal ER network structure (Sree et al., 2021), a comprehensive quantitative framework describing organelle scaling and population dynamics in myelinated axons seemed less developed.

Methodological innovations continue to enhance our capacity for organelle mapping: for example, the hybrid procedure developed by Jiang et al. (2025) demonstrates high efficiency in cell-wide reconstruction and quantification of mitochondrial networks across various specimens, including brain tissue. Their work highlights the utility of AI-assisted methods for large-scale analysis of a single, complex organelle network. Our approach complements this by applying similar volumetric and AI-assisted segmentation methods (SBF-SEM) to perform a direct, comparative quantitative analysis of two essential organelles (ER and mitochondria) across a population of myelinated axons. Specifically, while Jiang et al.'s work addresses the efficiency of mapping mitochondrial networks within a cell, our study focuses on the scaling relationship between the ER and mitochondria, revealing that their abundance co-scales while their volumes and surface areas are independently regulated.

It is noteworthy that high-resolution 3D reconstructions of the entire ER network remain less prevalent than those of other organelles like mitochondria. This study therefore contributes by establishing and applying a validated pipeline for automated SBF-SEM reconstruction and rigorous statistical analysis, demonstrating the feasibility and utility of achieving robust quantitative measurements of the axonal ER architecture.

### 4.1. Observations on axonal organelle scaling

By examining densities (organelle count per $\mu m^3$ axon length), our data suggests that ER and mitochondrial abundance may scale coordinately across PNS axons, supported by a strong Pearson correlation ($r = 0.79$; Fig. 6A). This robust correlation was confirmed by bootstrap analysis and maintains an extremely low Bonferroni-adjusted Q value ($8.1 \times 10^{-9}$), implying a global regulatory element ensuring both organelles are proportionally represented in larger axons, likely to support increased energetic demands.

In contrast, volume and surface area correlations between ER and mitochondria were negligible ($r \approx 0.03 - 0.04$), which might imply that organelle size is subject to more independent regulation through distinct biogenetic pathways. This differentiation between co-regulated abundance and independently regulated size is a key observation of our study.

The analysis of individual organelle morphology using power-law scaling (Fig. 7A) revealed exponents greater than the isometric expectation ($k_{Mito} = 0.85$; $k_{ER} = 0.73$). This result was confirmed with high confidence ($R^2 \approx 0.95$) and statistical certainty (Bonferroni-adjusted Q value of $8.31 \times 10^{-9}$). This super-isometric expansion points toward a structural adaptation where larger organelles prioritize increased membrane surface relative to volume. For mitochondria, this may reflect structural optimization for enhanced metabolic capacity, such as maximizing the surface area of the inner cristae. For the ER, it suggests an adoption of more complex or elongated morphologies, optimizing membrane surface for local calcium handling or signaling.

Furthermore, a critical observation concerns the low correlation of axonal length with most organelle metrics ($r_{length}$ vs $r_{volume} = 0.07$). This quantitative evidence lends support to the idea that local axonal size (cross-sectional area), rather than total axonal extent, is a more direct factor governing organelle content.

### 4.2. Methodological considerations and limitations

Limitations of this structural study must be acknowledged:

Resolution Trade-off and Contact Sites: First, this investigation did not include quantification of close contact-site distances ($\leq$ 30 nm apposition), which are commonly used to define functional Mitochondria-Associated Membranes (MAMs). This was a deliberate methodological choice: the resolution and large volume capability of our SBF-SEM dataset were optimized for capturing robust global scaling relationships across many axons, rather than the nanometer-precise contact measurements necessary to quantitatively confirm MAM distances. While our 3D reconstructions visually demonstrate the extensive and close entanglement of ER and mitochondria within the axon, a morphology that is highly suggestive of frequent close-range appositions, confirming distances $\leq$ 30 nm remains a necessary step for future studies employing techniques with ultra-high resolution (e.g., FIB-SEM, Cryo-ET). However, the observed co-scaling of organelle densities already offers strong structural evidence for coordinated regulation,

laying a foundation for these subsequent high-resolution investigations.

Sample Scope and Generalizability: The dataset is derived from a single Balb/c mouse sciatic nerve sample and includes 35 myelinated axons within a 17.65 μm-thick volume. While bootstrap analyses confirmed the robustness of observed correlations, the generalizability of these findings to other animals, nerve regions, or central nervous system axons remains to be established.

Structural *vs.* Functional Inference: Our study is structural by design, and functional inferences (e.g., regarding metabolic optimization) remain speculative until supported by complementary physiological assays.

Segmentation Quality: Although AI-assisted segmentation improves throughput and reproducibility, segmentation quality can still vary between organelles and requires careful manual validation.

Despite these limitations, this study illustrates the potential of combining volumetric EM, AI-assisted segmentation, and statistical methods to explore axonal scaling principles using a demonstrably capable pipeline. By distinguishing between abundance co-regulation and size independence, we offer a quantitative perspective that may inform subsequent investigations into ER–mitochondria organization in neuronal contexts. Future work combining 3D EM with functional imaging across broader sampling will be helpful in further elucidating the interplay between the axonal ER and mitochondria.

## 5. Conclusions

This proof-of-principle study used volumetric SBF-SEM and AI-assisted segmentation to provide a quantitative framework for analyzing Endoplasmic Reticulum (ER) and mitochondria within myelinated PNS axons.

We demonstrated that ER and mitochondrial abundance co-scale robustly with axon cross-sectional size, indicated by a strong Pearson correlation that maintains an extremely low Bonferroni-adjusted Q value ($8.1 \times 10^{-9}$). This suggests a coordinated regulatory mechanism for organelle number. In contrast, organelle volume and surface area correlations between the two organelles were negligible, implying independent regulation of size.

Analysis of individual organelle scaling revealed super-isometric expansion for both ER ($k_{ER} = 0.73$) and mitochondria ($k_{Mito} = 0.85$). This finding, confirmed with high statistical confidence (Bonferroni-adjusted Q value of $8.31 \times 10^{-9}$), points toward structural plasticity that prioritizes membrane surface area relative to volume as organelles enlarge. Furthermore, the limited influence of axon length on organelle content suggests that regulation is primarily a local phenomenon.

While limited to a single peripheral nerve sample, these findings establish a statistically robust quantitative framework for linking organelle organization to axonal size. This work offers a structural basis for understanding the interdependence of the ER and mitochondrial systems and provides a roadmap for future investigations that can incorporate larger datasets, central nervous system axons, and distance-based analysis of functional MAMs.

## CRediT authorship contribution statement

**Vitalijs Borisovs:** Writing – review & editing, Writing – original draft, Visualization, Software, Investigation, Formal analysis. **Mario Bossi:** Methodology, Investigation, Formal analysis, Data curation. **Guido Cavaletti:** Writing – review & editing, Supervision, Resources, Project administration, Funding acquisition, Data curation, Conceptualization.

## Declaration of Competing Interest

The authors declare that they have no known competing financial interests or personal relationships that could have appeared to influence the work reported in this paper.

## Acknowledgements

This work was performed within the National Plan for NRRP Complementary Investments (PNC, established with the decree-law May 6, 2021, n. 59, converted by law n. 101 of 2021) in the call for the funding of Research Initiatives for Technologies and Innovative Trajectories in the health and care sectors (Directorial Decree n. 931 of June 6, 2022)—project n. PNC0000003—Advanced Technologies (P.I. Guido Cavaletti).

## Appendix A. Supporting information

Supplementary data associated with this article can be found in the online version at doi:10.1016/j.micron.2025.103981.

## Data availability

Data will be made available on request.

## References

Clapham, D.E., 2007. Calcium signaling. Cell 131, 1047–1058. https://doi.org/10.1016/j.cell.2007.11.028.

Denk, W., Horstmann, H., 2004. Serial block-face scanning electron microscopy to reconstruct three-dimensional tissue nanostructure. PLoS Biol. 2, e329. https://doi.org/10.1371/journal.pbio.0020329.

Dittmer, P.J., Dell'Acqua, M.L., 2024. L-type $Ca^{2+}$ channel activation of STIM1-Orai1 signaling remodels the dendritic spine ER to maintain long-term structural plasticity. Proc. Natl. Acad. Sci. 121, e2407324121. https://doi.org/10.1073/pnas.2407324121.

Hetz, C., 2012. The unfolded protein response: controlling cell fate decisions under ER stress and beyond. Nat. Rev. Mol. Cell Biol. 13, 89–102. https://doi.org/10.1038/nrm3270.

Jiang, Y., Li, L., Chen, X., Liu, J., Yuan, J., Xie, Q., Han, H., 2021. Three-dimensional ATUM-SEM reconstruction and analysis of hepatic endoplasmic reticulum-organelle interactions. J. Mol. Cell Biol. 13, 636–645. https://doi.org/10.1093/jmcb/mjab032.

Jiang, Y., Wang, H., Boergens, K.M., Rzepka, N., Wang, F., Hua, T., 2025. Efficient cell-wide mapping of mitochondria in electron microscopic volumes using webKnossos, 2667-2375 Cell Rep. Methods 5 (2). https://doi.org/10.1016/j.crmeth.2025.100989.

Kasthuri, N., Hayworth, K.J., Berger, D.R., Schalek, R.L., Conchello, J.A., Knowles-Barley, S., Lee, D., Vázquez-Reina, A., Kaynig, V., Jones, T.R., Roberts, M., Morgan, J.L., Tapia, J.C., Seung, H.S., Roncal, W.G., Vogelstein, J.T., Burns, R., Sussman, D.L., Priebe, C.E., Pfister, H., Lichtman, J.W., 2015. Saturated reconstruction of a volume of neocortex. Cell 162, 648–661. https://doi.org/10.1016/j.cell.2015.06.054.

Kuijpers, M., Nguyen, P.T., Haucke, V., 2024. The endoplasmic reticulum and its contacts: emerging roles in axon development, neurotransmission, and degeneration. Neurosci. Rev. J. Bringing Neurobiol. Neurol. Psychiatry 30, 545–559. https://doi.org/10.1177/10738584231162810.

Lauwereyns, J., Bajramovic, J., Bert, B., Camenzind, S., De Kock, J., Elezović, A., Erden, S., Gonzalez-Uarquin, F., Ulman, Y.I., Hoffmann, O.I., Kitsara, M., Kostomitsopoulos, N., Neuhaus, W., Petit-Demouliere, B., Pollo, S., Riso, B., Schober, S., Sotiropoulos, A., Thomas, A., Vitale, A., Wilflingseder, D., Ahluwalia, A., 2024. Toward a common interpretation of the 3Rs principles in animal research. Lab Anim. 53, 347–350. https://doi.org/10.1038/s41684-024-01476-2.

Liu, J., Li, L., Yang, Y., Hong, B., Chen, X., Xie, Q., Han, H., 2020. Automatic reconstruction of mitochondria and endoplasmic reticulum in electron microscopy volumes by deep learning. Front. Neurosci. 14, 599. https://doi.org/10.3389/fnins.2020.00599.

Maiellano, G., Scandella, L., Francolini, M., 2023b. Exploiting volume electron microscopy to investigate structural plasticity and stability of the postsynaptic compartment of central synapses. Front. Cell. Neurosci. 17, 1153593. https://doi.org/10.3389/fncel.2023.1153593.

Maiellano, G., Scandella, L., Francolini, M., 2023a. Exploiting volume electron microscopy to investigate structural plasticity and stability of the postsynaptic compartment of central synapses. Front. Cell. Neurosci. 17. https://doi.org/10.3389/fncel.2023.1153593.

Moscardini, A., Di Pietro, S., Signore, G., Parlanti, P., Santi, M., Gemmi, M., Cappello, V., 2020. Uranium-free X solution: a new generation contrast agent for biological samples ultrastructure. Sci. Rep. 10, 11540. https://doi.org/10.1038/s41598-020-68405-4.

National Research Council, 1996. Guide for the care and use of laboratory animals. NRC, National Academy Press, Washington, DC.

Pfeffer, S., Brandt, F., Hrabe, T., Lang, S., Eibauer, M., Zimmermann, R., Förster, F., 2012. Structure and 3D arrangement of endoplasmic reticulum membrane-associated ribosomes. Struct. Lond. Engl. 1993 20, 1508–1518. https://doi.org/10.1016/j.str.2012.06.010.

Rowland, A.A., Voeltz, G.K., 2012. Endoplasmic reticulum–mitochondria contacts: function of the junction. Nat. Rev. Mol. Cell Biol. 13, 607–625. https://doi.org/10.1038/nrm3440.

Sree, S., Parkkinen, I., Their, A., Airavaara, M., Jokitalo, E., 2021. Morphological heterogeneity of the endoplasmic reticulum within neurons and its implications in neurodegeneration. Cells 10, 970. https://doi.org/10.3390/cells10050970.

Tafti, A.P., Kirkpatrick, A.B., Alavi, Z., Owen, H.A., Yu, Z., 2015. Recent advances in 3D SEM surface reconstruction. Micron Oxf. Engl. 1993 78, 54–66. https://doi.org/10.1016/j.micron.2015.07.005.

Vance, J.E., 2014. MAM (mitochondria-associated membranes) in mammalian cells: lipids and beyond. Biochim. Biophys. Acta 1841, 595–609. https://doi.org/10.1016/j.bbalip.2013.11.014.

Verkhratsky, A., 2004. Endoplasmic reticulum calcium signaling in nerve cells. Biol. Res. 37, 693–699. https://doi.org/10.4067/s0716-97602004000400027.

Wu, H., Carvalho, P., Voeltz, G.K., 2018. Here, there and everywhere: the importance of ER membrane contact sites. Science 361, eaan5835. https://doi.org/10.1126/science.aan5835.

Wu, Y., Whiteus, C., Xu, C.S., Hayworth, K.J., Weinberg, R.J., Hess, H.F., De Camilli, P., 2017. Contacts between the endoplasmic reticulum and other membranes in neurons. Proc. Natl. Acad. Sci. 114, E4859–E4867. https://doi.org/10.1073/pnas.1701078114.